

MULTIDISCIPLINARY CFD/CSD ANALYSIS OF THE SMART ACTIVE FLAP ROTOR

Mark Potsdam Mark V. Fulton
U.S. Army Aeroflightdynamics Directorate (AMRDEC)
Research, Development, and Engineering Command
Moffett Field, CA
{mark.potsdam, mark.v.fulton}@us.army.mil

Arsenio Dimanlig
Eloret Corp.
Moffett Field, CA
arsenio.dimanlig@us.army.mil

ABSTRACT

To address the complex multidisciplinary nature of rotorcraft analysis, high-fidelity computational fluid and structural dynamics models have been developed and coupled for an advanced technology active rotor. Significant advancements have been made in both modeling disciplines to allow for complex bearingless flapped rotors. Comparisons are made between CFD/CSD and comprehensive (lifting-line, free-wake) analyses and experimental data for the Boeing SMART rotor. Flap phase sweeps for 0, 2, 3, 4, and 5/rev flap inputs are investigated in relation to the zero flap deflection baseline at a nominal cruise condition. Changes in performance, aerodynamic and structural loads, control power, and noise are studied. Details of the high-fidelity flowfield solution, including flap gap effects and wake visualizations, are also presented.

INTRODUCTION

A range of advanced technology rotor concepts have been proposed to address important rotorcraft characteristics, such as noise (in-plane and blade-vortex interaction), vibration, loads, performance (payload, range, and speed), and stability and control. Active concepts include higher harmonic control, individual blade control, active flaps, active twist, and active flow control. Recent efforts have seen a wide range of research, using rotorcraft comprehensive analyses (Refs. 1-4) and computational fluid dynamics tools (Refs. 5-11), on the modeling of active rotor concepts with trailing edge flaps. In particular, under the DARPA Helicopter Quieting Program Phase IB, an active flap rotor was the focus of advanced tool correlation (8, 9). The Boeing SMART rotor used in that campaign provides a wealth of noise, loads, and performance data for validation of analysis tools on a full-scale, flapped rotor configuration. These analyses, along with wind tunnel tests of several flapped rotor configurations (Refs. 12-15) have shown that performance, vibration, and noise improvements are obtainable.

Analysis of helicopter rotors is a challenging multidisciplinary problem. Successful aerodynamic analysis requires accurate capabilities for modeling unsteady three-dimensional flowfields, transonic flow, reversed flow, dynamic stall, discrete vortical wakes, and complex geometries. This must be coupled with multibody, nonlinear structural dynamics analysis to provide elastic blade motion and rotor trim. These couplings in turn influence the full range of multidisciplinary rotorcraft characteristics.

The objective of this work is to apply state-of-the-art, loosely-coupled computational fluid dynamics (CFD) and computational structural dynamics (CSD) analysis to investigate the challenging problems of advanced technology active rotors. Rotorcraft CFD and CFD/CSD

coupling methods have made significant advancement in the past few years (Refs. 16-18), showing marked improvements over comprehensive analyses and their limited lifting line and free wake models. Compared with many previous CFD investigations (e.g. 6, 8, and 11), this work uses a high-fidelity Navier-Stokes CFD model of the SMART flapped rotor, including flap gaps and hub. For a baseline cruise condition and a range of flap input schedules, the CFD/CSD analysis is used to demonstrate and benchmark multidisciplinary prediction capability for aerodynamic and structural loads, rotor performance, in-plane noise, control power, and flow physics. Results are compared against comprehensive analysis (CA) and experimental test data.

SMART ROTOR CONFIGURATION

The Boeing SMART (Smart Material Actuated Rotor Technology) rotor was developed to demonstrate significant reductions in noise (in-plane and blade-vortex interaction) and rotor-induced vibration, and improved aerodynamic performance. It is a full-scale five-bladed bearingless MD900 helicopter rotor with piezoelectrically actuated flaps (Figure 1).

The rotor has a radius (R) of 16.925 ft. The blade consists of HH-10 and HH-06 airfoil sections with a linear twist of -10 degrees and a constant 10 inch chord. Starting at 93% R , the tip has a parabolic leading edge (22 deg sweep at the tip) with a straight trailing edge and 2:1 taper. Thrust-weighted solidity (σ) is 0.075. Nominal rotation speed is 392 RPM (0.62 hover tip Mach number).

The flap is centered at 83% R , extending from 74 to 92% R . The total flap chord is 3.5 inches (35% of total chord). The five equally-spaced flap hinges are located at 75% of the total chord, resulting in an effective flap/chord ratio of 25% with a 1-inch leading edge overhang. The flap is driven by a double X-frame actuator. The flap deflection, δ_r , on the k^{th} blade at azimuth angle ψ for the n^{th} frequency, with phase ϕ is

$$\delta_{jk} = A_n \sin(n\psi_k + \phi_n)$$

Flap deflections are positive trailing edge down.

Report Documentation Page			Form Approved OMB No. 0704-0188					
<p>Public reporting burden for the collection of information is estimated to average 1 hour per response, including the time for reviewing instructions, searching existing data sources, gathering and maintaining the data needed, and completing and reviewing the collection of information. Send comments regarding this burden estimate or any other aspect of this collection of information, including suggestions for reducing this burden, to Washington Headquarters Services, Directorate for Information Operations and Reports, 1215 Jefferson Davis Highway, Suite 1204, Arlington VA 22202-4302. Respondents should be aware that notwithstanding any other provision of law, no person shall be subject to a penalty for failing to comply with a collection of information if it does not display a currently valid OMB control number.</p>								
1. REPORT DATE MAY 2010	2. REPORT TYPE	3. DATES COVERED 00-00-2010 to 00-00-2010						
4. TITLE AND SUBTITLE Multidisciplinary CFD/CSD Analysis of the Smart Active Flap Rotor			5a. CONTRACT NUMBER					
			5b. GRANT NUMBER					
			5c. PROGRAM ELEMENT NUMBER					
6. AUTHOR(S)			5d. PROJECT NUMBER					
			5e. TASK NUMBER					
			5f. WORK UNIT NUMBER					
7. PERFORMING ORGANIZATION NAME(S) AND ADDRESS(ES) U.S. Army Aeroflightdynamics Directorate (AMRDEC), Research, Development, and Engineering Command, Moffett Field, CA, 94035			8. PERFORMING ORGANIZATION REPORT NUMBER					
9. SPONSORING/MONITORING AGENCY NAME(S) AND ADDRESS(ES)			10. SPONSOR/MONITOR'S ACRONYM(S)					
			11. SPONSOR/MONITOR'S REPORT NUMBER(S)					
12. DISTRIBUTION/AVAILABILITY STATEMENT Approved for public release; distribution unlimited								
13. SUPPLEMENTARY NOTES								
14. ABSTRACT <p>To address the complex multidisciplinary nature of rotorcraft analysis, high-fidelity computational fluid and structural dynamics models have been developed and coupled for an advanced technology active rotor. Significant advancements have been made in both modeling disciplines to allow for complex bearingless flapped rotors. Comparisons are made between CFD/CSD and comprehensive (lifting-line, free-wake) analyses and experimental data for the Boeing SMART rotor. Flap phase sweeps for 0, 2, 3, 4, and 5/rev flap inputs are investigated in relation to the zero flap deflection baseline at a nominal cruise condition. Changes in performance, aerodynamic and structural loads, control power, and noise are studied. Details of the high-fidelity flowfield solution, including flap gap effects and wake visualizations, are also presented.</p>								
15. SUBJECT TERMS								
16. SECURITY CLASSIFICATION OF: <table border="1"> <tr> <td>a. REPORT unclassified</td> <td>b. ABSTRACT unclassified</td> <td>c. THIS PAGE unclassified</td> </tr> </table>			a. REPORT unclassified	b. ABSTRACT unclassified	c. THIS PAGE unclassified	17. LIMITATION OF ABSTRACT Same as Report (SAR)	18. NUMBER OF PAGES 22	19a. NAME OF RESPONSIBLE PERSON
a. REPORT unclassified	b. ABSTRACT unclassified	c. THIS PAGE unclassified						

Initial functionality and capability of the active flap system was demonstrated in a 2003 Boeing whirl tower test. During 2008, an extensive test campaign was successfully performed by a team from Boeing, DARPA, NASA, Army, Air Force, MIT, UCLA, and the Univ. of Maryland in the Air Force National Full-Scale Aerodynamics Complex (NFAC) 40- by 80-Ft. Wind Tunnel at the NASA Ames Research Center (Ref. 12) (Figure 2). The 11-week test gathered data for a range of forward flight conditions using open- and closed-loop flap control (Ref. 19). A similar unflapped MD900 MDART (McDonnell Douglas Advanced Rotor Technology) rotor was tested previously in the NFAC in 1992 with higher harmonic control (Ref. 20). SMART rotor instrumentation includes flap bending, chord bending, and torsion moments at several radial stations on the blade; pitch link loads; five-component rotor balance measurements; and rotor torque. Acoustic measurements are made using an array of microphones placed in the acoustically-treated test section.

METHODOLOGY

The SMART rotor is a complex configuration from a geometric, structural, and aerodynamic modeling perspective. Both the CSD and CFD models required significant development efforts, which are described here.

CSD

The computational structural dynamics (CSD) calculations for the SMART rotor use the CAMRAD II v4.6 (Ref. 21) comprehensive rotocraft analysis software. The input is a derivative of a baseline model provided to the DARPA Helicopter Quieting Program participants by Boeing/NASA.

The baseline model represents the bearingless rotor blade with a dual load path for the pitchcase and the flexbeam. Each blade is represented by 5 beam elements – from the root of the pitchcase to the tip of the blade – plus 5 beam elements for the flexbeam. Baseline structural properties were used for the flexbeam, pitchcase, and blade. The hub and swashplate are rigid, but the pitch links have a linear compliance.

A derivative of the baseline model was created to enable CFD/CSD coupling. Most significantly, the trailing edge flap was modified from a single rigid body to an elastic beam model with multiple hinge supports. In particular, two beams are cantilevered together to form one continuous flap. It is supported by five hinges, similar to the experimental hardware. Each hinge allows three rotational degrees of freedom but provides linear displacement constraints in two directions, normal (vertical) and chordwise. The second hinge also constrains the flap in the axial (blade radial) direction to carry centrifugal force. Actuator input is provided at the base of a torsional spring that is attached to the second joint pitch degree of freedom, although the experimental model has the control rod attachment at the first (inboard) hinge. Nominal rotational springs were included at each joint for flap and chord rotations. For these calculations, the flap

was made rigid in torsion and in the axial (blade radial) direction. The flexibility of the flap was retained, though, in flap- and chord- bending, to allow it to more closely conform to the main blade shape, thus better preserving the gap geometry. Creation of the flap model – especially the structure, response, and output – required a significant amount of CAMRAD II core input, which is significantly more difficult than shell input used for conventional configurations.

The aerodynamics is modeled using a lifting-line model and airfoil table look-up, with 20 aerodynamic panels. A tip loss correction is not used. Flap aerodynamic increments are applied to the main airfoil. The unsteady aerodynamics is modeled with a sealed gap. A free wake model is used for comprehensive analysis calculations, but linear inflow is used with CFD/CSD coupling. The free wake model is a single peak with two revolutions of wake. Therefore, the flap end effects are ignored.

A harmonic solution is performed using modal analysis. Eighteen blade modes are retained, as this number was found to be sufficiently accurate while having good convergence characteristics for CFD/CSD coupling. Modal damping of 2% critical is used.

Structural convergence was found to be sensitive to a number of solution parameters. First, the flexbeam model is reduced to one axial degree of freedom, which eliminated a numerical issue with the spring matrix. This strategy is consistent with general CAMRAD II modeling guidelines regarding bearingless rotors, and should be a good approximation for the flexbeam. Second, a small relaxation factor is used for the rotor part solution, which appears to eliminate numerical divergence difficulties and provides for an accurate calculation of the rotor thrust and the snubber vertical deflection. Third, for startup, the SMART snubber linear properties are replaced with the MDART snubber properties, with the SMART properties used for the final converged result. The MDART snubber has linear stiffnesses and damping that are 80% and 30% larger, respectively. It seems that this final change explains why the SMART numerical model has been less robust than MDART.

Previous calculations on the SMART rotor have been performed using CAMRAD II comprehensive analysis (Ref. 2). Structural load comparisons have generally been fair.

CFD

CFD calculations use the complex geometry Navier-Stokes CFD solver OVERFLOW 2.0aa, enhanced under a DoD CHSSI Portfolio, Collaborative Simulation and Testing (CST-05) (Ref. 22). OVERFLOW computes solutions on structured, overset grids using a near- and off-body discretization paradigm. Time-accurate simulations of complex aircraft configurations with aeroelastic bodies in relative motion can be efficiently computed on parallel processors using the MPI Message Passing Interface.

The SMART surface and volume grid configuration is shown in Figures 3 and 4 (coarse grid). The high-

fidelity surface mesh modeling includes the rotor blade, pitchcase and damper caps, tracking tab, flap, hub, and PCM fairing. The discrete flap gaps have been faithfully duplicated without reverting to ad-hoc boundary conditions or flow-through surface approximations. The flap hinges and actuators have not been modeled. Figure 3 shows the overset surface grid topology used at the flap gap edges. Manual I-Blanking has been employed for the truncated section of the main airfoil. Figure 4 shows the volume grid topology with hole cutting at the spanwise and chordwise flap gaps.

Due to the small gap spacing between the main blade and flap (0.1 inches spanwise, 0.07 inches chordwise) and the difficulty in performing the domain connectivity in this region (Figure 4), modifications were performed to the basic x-ray hole-cutting scheme in OVERFLOW to improve accuracy, memory footprint, and parallel efficiency. Otherwise, the computational requirements can become prohibitive (Ref. 23). The small gaps required very small x-ray spacing to replicate the geometry in this region. Due to computer memory limitations, it was not feasible to x-ray the entire blade at this resolution. Special purpose x-rays of the flap gaps were created. To further reduce the size of these special x-rays, their spatial extent in the plane of the rotor was tied to the aeroelastic motions of the blades. Because of the special x-rays which need to be regenerated every step, the standard x-rays for the entire blade and flap, and the x-rays in the hub region, the amount of on-the-fly x-ray regeneration increased significantly. The regeneration process was parallelized for increased computational efficiency. These improvements resulted in active flap domain connectivity times of 10-20% of a flow solver step, which is consistent with conventional rotors without high-fidelity active controls (Ref. 16). X-ray storage requires 186 MB.

Both coarse and fine grids have been developed. They are detailed in Table 1. Most results herein use the coarse grid, with spot checks using the fine grid. The portion of the blade without the flap is made up of 8 grids (root cap, pitchcase, inboard of the flap, flap region, outboard of the flap, tip cap, and inboard and outboard flap gap end caps). The flap is made up of 3 grids (flap, inboard and outboard tip caps). The grids are O-grid topology, with 21 points across the blunt trailing edge fine grid. The Cartesian level 1 (L1) off-body mesh surrounds the rotor and captures the wake. Coarse grid coupled solutions can be obtained overnight with 95% parallel efficiency on a Cray XT5. The CAMRAD II CSD serial portion of the coupling is minimal, requiring 90 seconds per coupling

iteration (< 1.5% of the total for coarse grid analyses).

The time-accurate calculations use a 4th-order central difference spatial discretization with added 4th-difference scalar (near-body) and matrix (off-body) artificial dissipation, resulting in a 3rd-order scheme. A 2nd-order temporal backward difference scheme with iterative dual-time stepping is used for time advancement. Twenty (20) subiterations are used on the fine grid and 10 subiterations on the coarse grid, typically resulting in 1.5 – 2.0 orders of magnitude reduction in the main blade grid residuals. Quarter degree (0.25°) time steps are used (1440 steps per rotor revolution). The Spalart-Allmaras turbulence model is employed in the near-body grids. The off-body wake grids are inviscid.

CFD/CSD Coupling

CFD/CSD coupling is performed using a conventional (for rotorcraft) loose coupling incremental “delta” formulation (e.g. Ref. 16). Coupling is on a per revolution basis based on periodicity. Motions (3 rotations and 3 translations of the airfoil sections) and airloads (section normal force, chord force, and pitching moment) are exchanged. Fully-automated coupling is performed using shell scripting, file I/O, and fluid-structure interface programs. For the active flap rotor, the main blade and flap are treated as two separate “rotors” within OVERFLOW. Airloads integration and motion specification are applied separately. This “dual-rotor” concept would not work for integral active device concepts, for which the separation between components is not distinct.

Considerable care was necessary to ensure that the CFD and CSD models were consistent with each other, particularly with respect to reference coordinate systems, planform layout, and hinge locations. This was especially important in order to avoid intersection of the flap and main blade in the gap region. Different resolution of the geometries in the CFD and CSD domains make this task particularly difficult.

Typically, 7 coupling iterations are used, with 2/5 rev between each coupling. Therefore, a coupled solution requires ~4 complete rotor revolutions, including the initial starting revolution. As discussed previously, the bearingless rotor structural model is somewhat ill-conditioned compared with articulated models, so that convergence of CFD airloads and CSD rotor trim controls and aeroelastics is not as tight (Ref. 16), but still within acceptable engineering accuracy. Hub and pitchcase

Table 1. SMART grid characteristics and dimensions

Grid	blade	flap	Near-body points per blade	Off-body L1 spacing	% off-body points	Total points	Hours per rotor revolution	processors
	dimensions: chord x span x normal							
Fine	221 x 305 x 59	169 x 61 x 59	4.9 M	8% chord (0.8 inch)	60	66.5 M	13.2	320
Coarse	Every other point of fine mesh		820,000	12% chord (1.2 inch)	75	17.0 M	4.2	128

turbulence also contribute to degraded convergence and imperfect periodicity. An example convergence plot of blade control pitch angles (collective, θ_0 ; lateral cyclic, θ_{lc} ; longitudinal cyclic, θ_{ls}), CFD thrust, CFD torque, and section aerodynamic normal force ($M^2 c_n$) at 84% span (mid-flap) are shown in Figure 5 for baseline flow conditions and zero flap deflection. The lateral cyclic pitch appears unconverged but, in actuality, only varies by 0.03 deg. The flap deflection cases are initiated from the baseline (zero flap) case and show similar convergence.

CAMRAD II requires both the total section airload (main plus flap) in the region of the flap as well as the flap-alone airload. The CFD/CSD interface code must supply the total sectional airload based on a vectoral summation of discrete main and flap airloads provided by the CFD solver. In turn, CAMRAD II provides motion of both the main portion of the blade and the flap. The motion of the main portion of the blade is relative to the undeformed quarter chord. Because the main blade chord in the region of the flap is truncated, special care must be taken in specifying the actual quarter chord of the blade to CFD, which in general has no notion of the total blade planform. The motion of the flap provided by CSD is specified relative to the flap hinge. The flap hinge reference point is specified as input in both CSD and CFD for the flap motion and the flap section pitching moment calculation. Figure 6 shows an example of the CSD calculated main blade and flap section pitch motion for a 5P flap, 1.5 deg deflection input at the second flap hinge (83% R). The difference in torsion motion between the two components is the specified flap motion.

RESULTS

In this work, most results correspond to a moderate cruise speed, level flight test condition: 123 kts, 0.3 advance ratio, 0.075 thrust level (C_T/σ), -9.1 deg shaft angle (nose down). The nominal trim condition is the thrust target and zero flexbeam cyclic flap bending moments, used to determine the blade collective and cyclic pitch angles. The shaft angle is held fixed. Comparison of the control angles for the baseline (no flap deflection) case are shown in Table 2. They are seen to be in excellent agreement with the test data. The absolute torque comparison of the baseline case is also shown to be in reasonable agreement, with excellent agreement for the fine grid, although grid convergence cannot be claimed. The forces and moments from CFD include all the solid surfaces (blades, flaps, pitchcase, hub, PCM). This is consistent with the test data used, which has only been corrected for blade and hub weight and rotational tares, and not for aerodynamic tares.

Active rotor CFD/CSD calculations have been obtained for flap harmonics of 0, 2, 3, 4, and 5/rev (0P, 2P, 3P, 4P, 5P), a nominal flap amplitude of 1.5 deg, and a sweep of flap phase angle (ϕ) and flap amplitude (0 and 2P). 0P inputs correspond to static flap deflection. For all the analyses the rotor is re-trimmed to maintain the specified thrust and zero flexbeam cyclic flap bending. This results in a more realistic determination of the

advantages of the flap inputs, although it complicates comparisons with experimental data which were not re-trimmed for the 3, 4, and 5P flap harmonics. Additionally, in the 2P case, the controls are held fixed at the baseline values for the flap phase sweep, although aeroelastic effects due to the motion of the active flap must still be included with CFD/CSD coupling. This allows direct comparison with 2P test data. Also in the 2P input case, higher thrust ($C_T/\sigma = 0.090$), higher advance ratio ($\mu = 0.38$), and varying flap deflection ($\delta_f = 0.5 - 3.0$ deg) have been computed in search of optimal performance improvements. Results are compared against SMART wind tunnel test data and CAMRAD II free-wake lifting-line analysis, as available.

In the following sections the SMART calculations will be compared against experimental data for prediction of:

- 1) structural loads
- 2) control power
- 3) performance
- 4) in-plane noise

First, aerodynamic details will be investigated, even though no experimental aerodynamic validation data is available for surface and flowfield results.

Table 2. Baseline controls and performance:
 $C_T/\sigma = 0.075$, $\mu = 0.30$, $\alpha_s = -9.1^\circ$

	θ_0	θ_{ls}	θ_{lc}	C_T/σ	C_Q/σ
Test	10.3	-6.20	1.68	0.0749	0.00690
Fine grid	9.9	-6.16	1.83	0.0746	0.00685
Coarse grid	10.1	-6.14	1.84	0.0748	0.00724

Aerodynamics and Flow Physics

Airload comparisons between CFD/CSD and CA are shown in Figure 7 for the baseline case (zero flap deflection) and the untrimmed (fixed controls) 2P/1.5°/90° and 2P/1.5°/270° cases (flap harmonic/amplitude/phase). Total section normal and chord force, and pitching moment at 84% R (mid-flap) as a function of azimuth indicate several differences between the CFD and lifting-line aerodynamics, particularly on the advancing side. Pitching moments are in very good agreement except for negative flap deflection (positive pitching moment) and on the advancing side. Due to compressibility and three-dimensional effects, it is expected that the CFD results would more accurately model the physics. Chord force trends are well captured but are offset. Airloads differences between the coarse and fine grid results (not shown) are small, other than a minor shift in the chord force.

Comparison of normal force disk loadings on the baseline case in Figure 8 indicates that the lifting-line results tend to be more outboard loaded with a small phase shift. This is probably due to realistic 3D flap effects (e.g. leakage), as shown later.

Example airloads for 2-5/rev inputs are shown in Figure 9 for 0 deg flap phase, 1.5 deg deflection, along with airloads for the undeflected flap case. In all cases it is not difficult to pick out the n/rev content. Due to the moment inducing nature of the flap and aeroelastic coupling, the effect of the flap on the normal force is most noticeable at stations outboard of the flap. For normal and chord force, 95% span is shown. Pitching moment is shown at 84%.

CFD calculations afford the opportunity to visualize and investigate detailed on-surface and off-surface flow physics. Figure 10 shows a wake visualization using the Q criterion ($\|\Omega\|^2 - \|S\|^2$) for the fine grid, fixed controls, 2P/1.5°/90°. The Q iso-surface is colored by the sense of the vorticity vector relative to the rotor rotation (normalized $\omega \cdot (r \times \Omega)$). (This works best for younger wake ages.) The wake turbulence from the hub and pitchcase is significant. Rotor tip vortices are well defined and discrete. They indicate no negative loading on the advancing side. Flap end vortices can also be seen, depending on the phase of the flap deflection. For this case the flap is trailing edge down at 0 and 180 deg azimuth and up at 90 and 270 deg. At 0 deg azimuth both flap end vortices are clearly seen (above the hub turbulence) and are consistent with flap deflection down. At 72 and 288 deg azimuth (blades 2 and 5), the flap is deflected up, and the opposite sense of flap tip vortex rotation is seen.

The flow in the vicinity of the mid-span chordwise and inboard edgewise flap gaps at 0 deg azimuth are shown in Figure 11. Note that the surface velocities may not be zero due to the aeroelastic relative motions of the blade and flap, although rotor rotational motion has been subtracted. The velocity of the flap leading edge is noticeable (i.e. non-zero at the surface). The complexity of the flow is seen in the velocity vectors and pressure coefficient. The discontinuity and disjointedness in some of the contours highlight the complications of the overlapping grids and domain connectivity procedure in these regions (Figure 4) and point to resulting inaccuracies due to grid and overlap mismatch. Nonetheless, the flow is seen to be able to transit through the gaps and results in leakage between the upper and lower blade surfaces.

Flap Gap Effects

In addition to the high-fidelity flap modeling detailed in the Methodology section for the SMART rotor, an equivalent unflapped rotor has been developed. This configuration is labeled MDART after the NASA/McDonnell Douglas test of this unflapped pre-production MD-900 rotor (Ref. 20). It has the same aerodynamic contours as the SMART rotor, but with the flap gaps removed, no PCM fairing, and somewhat different blade structural properties. Due to the location of the flap, the trim tab on the SMART was moved inboard relative to the MDART location. Grid density between the two configurations is comparable. Comparing results between these two rotors clarifies the influence of the flap gaps on the aerodynamics. Three configurations are of

interest: 1) SMART rotor trimmed to baseline conditions, 2) MDART rotor trimmed to baseline conditions, and 3) MDART rotor using SMART rigid and aeroelastic blade motions including controls, as shown in Table 3.

Table 3. SMART and MDART comparisons

configuration	C_T/σ	C_Q/σ	θ_0
SMART	0.0748	0.007244	10.1
MDART	0.0745	0.007236	9.5
MDART (SMART motions)	0.0760	0.007348	10.1

For essentially the same thrust, the SMART rotor requires a 0.6 deg collective pitch increase. Alternatively, using the SMART aeroelastic deflections and control inputs, the MDART rotor produces 1.6% more thrust. Power comparisons using the coarse mesh indicate essentially the same power required by both rotors at constant thrust, which is somewhat surprising.

Figure 12 shows the mean normal and chord force distributions for the MDART and SMART rotors. The SMART rotor geometry with tab and flap location is shown for clarity. The large spikes between 70 and 80% span are the edges of the 4% span tabs for each configuration. The mean normal force distributions show that for the same thrust the MDART rotor is more outboard loaded. The SMART rotor shows reduced loading in the region of the flap which is made up for with inboard loading. Loading outboard of the flap is the same for MDART and SMART. For the MDART rotor with SMART motions, the loading in the region in the flap is increased compared with the SMART, but is the same as for the MDART. The extra thrust in this case comes from the inboard portion of the blade.

The CFD chord force convention is positive toward the leading edge (i.e. the drag direction is negative). This force is in the direction of the local chord, and is, therefore, not actually drag or x-force, which requires knowledge of local angle of attack or section twist. The mean chord force shows that the decreased SMART outboard loading is, nonetheless, associated with increased force in the direction of the trailing edge due to the flap. Significant chord forces are associated with the flap ends. The mean pitching moment (not shown) indicates that the undeflected flap contributes a small nose down moment compared with the unflapped section.

Figure 13 compares the baseline SMART mean normal force distribution for the CFD/CSD and comprehensive analyses. It is seen that the CA result is highly tip loaded. Referring to the CFD/CSD MDART results in Figure 12, the CA tip loading is higher than would be suggested by the fact that the lifting line and free wake analysis does not account for the flap gap and leakage. No tip loss correction is used in the CA model. This high tip loading may explain the improvements obtained with high Mach number corrections (Ref. 2). Experimental airloads data would certainly assist in evaluating aerodynamic prediction accuracy.

Control Power

For advanced rotor concepts it is important to quantify the control power, or the ability of the active flap to alter rotor loads and trim. A flap input at 0P (static) or 1P produces forces equivalent to swashplate collective and cyclic pitch.

Figure 14 shows CFD/CSD predicted control power for both 0P flap input and collective pitch input compared with test data. Both thrust and torque changes are plotted as a function of flap deflection or collective pitch change are plotted. There is generally good agreement between CFD and test, although small slope differences of about 10% for thrust changes with deflection exist. Torque as a function of deflection is well predicted. The SMART flap behaves as a moment flap in that positive flap deflection (trailing edge down) reduces the rotor thrust due to the resulting and overriding nose down blade twist. Consequently, negative flap deflection (flap up) is used to increase rotor thrust, and the flap deflection trends are opposite collective pitch inputs. A +3 deg flap deflection is approximately equivalent to a -0.6 deg collective pitch change.

Figure 15 shows thrust vs. torque for the collective pitch and flap deflection inputs. As noted previously there are minor slope mismatches between CFD/CSD and test. The local slope of the thrust-torque curve is higher for the collective input, indicating that small thrust increases can be made more efficiently with flap deflection than with collective, if actuator work is neglected.

Performance

In order to increase the payload, range, and speed of rotorcraft, it is important to be able to predict the rotor thrust, torque, and drag. Active controls have the potential to improve rotor performance. Past research has shown that 2/rev control inputs are particularly effective (Refs. 3, 7, 24).

The percentage power/thrust (P/T) improvement compared with the unflapped case, for 2P/1.5° as a function of flap phase, is shown in Figure 16 for the baseline flight conditions ($C_T/\sigma = 0.075$, $\mu = 0.30$, $\alpha = -9.1$ deg). Power over thrust is used to account for the variations in thrust, even when the rotor is nominally trimmed to constant thrust. However, lift over equivalent drag ratio would be a more appropriate metric given that the shaft angle is fixed. In this figure the rotor has not been re-trimmed at each different flap input, but rather the controls have been fixed at their baseline values. It is seen that the CFD/CSD, CA, and test data trends and magnitude are in good agreement, particularly with respect to the improvement in P/T. The optimal flap phase is around 90 deg. In the experiment, it was seen that with fixed controls the baseline test conditions wandered between the start and end of the phase sweep, as indicated. Fine and coarse grid CFD/CSD results are shown. Even though the magnitude of the power is grid dependent (Table 2), the percentage changes (increments) from the baseline are quite similar. This trend due to grid effects is generally maintained across the range of flap

phasing. Based on these results, most calculations in the remainder of the paper will use the coarse grid for efficiency reasons.

Because the rotor is not re-trimmed in this comparison, the effect on performance is mostly due to changes in thrust. The regions of increased normal force on the rotor disk compared with the baseline are shown in Figure 17 for the optimal phase angle. Local effects on the flap (74 – 92% R) are seen along with trends, outboard of the flap (> 92% R), related to flap-induced torsion.

In Figure 18 the rotor is re-trimmed to thrust and flexbeam flap bending moment at each flap phasing. The performance improvement is significantly smaller, although the trends with phase remain. The test data and the CFD analyses, in particular, would indicate that these improvements for the trimmed rotor are negligible (Ref. 12), except for the possible test point at 60 deg phase. On the other hand, no significant performance degradation is noted, in case the active flap is used for other purposes (noise, vibration). It is not clear why the CA results show no improvement at any flap phase.

The experimental variation for two test points at 0 and 360 deg phase are shown in the figure. They indicate an approximate error range of at least 1% for the experimental data. This may be in addition to the uncertainty in the repeatability of the baseline test point. The CFD results, even as increments from a baseline value, are also not accurate to less than the 1% improvement shown – convergence of the CSD, CFD, and CFD/CSD coupling do not meet such tight tolerances for this rotor. The baseline result from which the increments are taken also affects the increments. The grid convergence for the untrimmed 2P flap inputs (shown previously in Figure 15) adds to this error limitation. Overall, both the test data and CFD accuracy and repeatability were not less than 1% – for this configuration. However, these comparisons still provide some level of validation of the ability of the CFD/CSD results to capture flap performance trends.

Because 2P flap inputs were shown to be effective in the past, the rotor was simulated at several other flap amplitudes and flight conditions to determine if any significant improvement could be found (Figure 19). A sweep on flap amplitude at the baseline flight conditions and a higher thrust coefficient ($C_T/\sigma = 0.09$) at 90 deg phase indicates that the 1.5 deg deflection is optimal, and performance degrades for larger amplitudes. Analysis at a higher advance ratio ($\mu = 0.38$) indicates that negligible performance improvements are obtained. Higher flap harmonics (3, 4, and 5/rev) also produced no or negligible performance improvement (not shown). It is still possible, though, that alternative flap deflection waveforms could improve rotor performance. Further study along with comparisons with other rotors is required in order to determine why the SMART rotor performance was not improved.

Structural Loads

In order to design a rotor blade for a specified fatigue life and load limiting flight conditions, it is important to be able to accurately predict structural loads in the blade, flexbeam, pitchcase, and pitch links. The addition of active load-inducing controls onto a rotor has the possibility of increasing or decreasing rotor loads. Therefore, in addition to baseline loads, the maximum load increments produced by flap motion are investigated, with the latter being a measure of flap effectiveness.

The baseline structural loads at locations inboard of the flap are shown in Figure 20. Neither the flap bending (59% R) nor the torsion moment (64% R) is particularly well predicted for magnitude, phase, or higher frequency content. The chordwise bending moment (59% R) is in reasonable phase and higher harmonic agreement. Although the CFD/CSD result shows improvement over comprehensive analysis, the peak-to-peak magnitude is underpredicted. A Mach number correction factor was used by Kottapalli (Ref. 2) for the sectional pitching moment outboard of 74% R in CAMRAD II in order to improve the structural loads correlation. It was postulated that this was required due to compressibility effects, which CFD would more accurately capture. This appears to not be the case for the current calculations.

Figure 21 shows the azimuthal variation of the oscillatory structural load increments for experiment and CFD/CSD for the 5P/1.5°/90° case. The increments were calculated by subtracting the baseline azimuthal variation (Figure 20) from the 5P/1.5°/90° structural response. For the flap bending moment, the maximum magnitude and waveform are not entirely captured. The torsion moment comparison is in good agreement, with some phase and magnitude error. Note that the experiment and analysis both show a 1/rev variation in the torsion moment due to dynamic pressure variations around the disk. The CFD/CSD chord bending moment increment prediction is poor. It agrees in neither the maximum magnitude nor the waveform.

Measures of flap effectiveness are indicated in Figures 22 and 23, which show torsion and flap bending moment increments, respectively, as a function of blade span station, for both the test data and the CFD/CSD results. The upper portion of these figures shows the 0P response to 0P flap deflection, and the lower portion shows the 5P response to 5P flap deflection. These are the primary responses for a particular flap oscillation harmonic. The moment increments that are calculated are from the maximum magnitude at that harmonic – during an amplitude sweep (0P) or a phase sweep (5P) – minus the baseline magnitude (at the same harmonic). All results correspond to a 1.5° flap deflection. In general, the phase (not shown) for maximum load varies with span station. For reference, the phase for maximum CFD/CSD 5P torsion is 90° at 64% R, corresponding to the 5P/1.5°/90° case in Figure 21. Finally, in this plot consider the location of the sensors. For the torsion moment, the two inboard stations are on the pitchcase, with the remainder on the blade; for the flap bending moment, the inboard station is on the flexbeam, but the

next station is on the pitchcase, with the remainder on the blade.

The torsion moments in Figure 22 show that the CFD/CSD results match the test data much more closely for 0P (13% difference at 64% R) than for 5P (28% difference), although the trends are in reasonable agreement. The reason for this change with harmonic input is not known, though it could be caused by structural dynamics, aerodynamic damping, and/or flap aerodynamics. Figure 22 also shows that the torsion moment increment is bigger for 5P than for 0P. The larger 5P response includes significant dynamic amplification, due to the proximity of the first torsion mode at 5.8P. Figure 23 shows that the flap bending moment correlation is considerably worse.

Overall, the CFD/CSD structural load results shown are in fair to poor agreement with data, and suggest that CFD/CSD airloads do not improve the structural load correlation in comparison with unmodified CA results, indicating a need for further investigation. Improving the prediction accuracy of these loads should begin with a detailed examination of blade structural properties, dynamics, and aerodynamics.

In-plane Noise

For both military and civil operations, it is important to reduce the aural detection distance and noise signature of the vehicle to observers. Various rotor control devices have been able to favorably affect the rotor noise from both blade-vortex interactions and in-plane sources (Refs. 25, 26). The effect of flap harmonic, amplitude, and phase on in-plane noise has been recently evaluated for the SMART rotor (Ref. 25).

Noise signatures from the computational results are computed using the Ffowcs-Williams Hawkings (FW-H) acoustic analogy in the PSU-WOPWOP v3.3.3 code (Ref. 27). Farassat's Formulation 1A is employed. Non-compact surface loadings as a function of azimuth for a complete rotor revolution are converted from OVERFLOW (PLOT3D) surface pressures and output to PSU-WOPWOP format (Ref. 28). Although not used here, PSU-WOPWOP also has the capability to compute noise from permeable surfaces located in the flow field. Different noise signatures may be obtained depending on the use of the different noise sources (Ref. 9).

The experimental microphone location (SMART mic. 13) is 1.8R in front of and 0.6R towards the advancing side of the rotor hub, in the plane of the rotor taking into account the baseline shaft tilt (-9.1 deg). This is consistent with in-plane analysis (Figure 24). A Low Frequency Sound Pressure Level (LFSPL, dB) metric, containing up to 6 blade passage frequencies, is used to evaluate in-plane noise. Up to a 2.5 dB noise reduction in the LFSPL for the 2P phase sweep is shown in Figure 25a for both the CFD/CSD and experimental results, with a somewhat narrow optimal phasing around 0 deg. The experimental data and CFD/CSD results also indicate that whether the results are re-trimmed or not at each phase is not important. The results are in very good agreement. The LFSPL increments as a function of phase for the 3P

and 5P results are shown in Figure 25b,c. Again the magnitude and phasing of the results are in good agreement. However, it is clear that all the comparisons, and especially the 5P, would be noticeably improved with a ~ 30 deg shift in the flap phasing for the CFD/CSD results. There does not appear to be any phase reference error between CFD and test, and the commanded flap deflection between the two results has been verified (Figure 6). Although airloads comparisons would most easily help to explain the differences, mid-span torsional moments could be investigated for potential causes in presumably differing blade loads. 4P results are in similar agreement but are not shown due to flap deflection limitations in the test (1.0 deg), compared with the 1.5 deg deflection for the CFD/CSD results.

Figure 26 shows the acoustic pressure signature for the baseline case. Table 4 compares the integrated OASPL and LFSPL. The comparison with data is quite poor, as the minimum peak pressure is underpredicted by ~ 12 Pascals and the LFSPL by 6 dB. The experimental data for a case with slightly higher thrust ($C_T/\sigma = 0.080$) is also shown for comparison. The peak pressures are quite different as a function of thrust. CFD/CSD analyses of these two thrust levels do not capture this trend (Ref. 29). The individual thickness and loading contributions from CFD/CSD are also shown in Figure 26. It is seen that the peak thickness pulse is cancelled by the loading noise, resulting in reduced peak magnitude. Apparently this is not the case for the measured data, or possibly the thickness noise from FW-H is underpredicted. Currently, the reason for this glaring discrepancy is not known. It should be noted that other on-surface analyses have predicted similar results (Refs. 9, 30). However, off-surface methods such as direct CFD acoustic predictions (Ref. 29) and permeable surface FW-H (Ref. 9) produce better agreement than the on-surface methods, although separation of thickness and loading noise is no longer possible. It is suspected that non-linear off-surface noise sources are involved. Overall, even though the LFSPL noise increments (dB) can be well captured using on-surface methods, the absolute noise levels are poorly predicted.

**Table 4. Baseline noise SPL comparisons:
microphone 13**

	OASPL (dB)	LFSPL (dB)
Experiment	110.0	109.8
CFD/CSD	104.7	103.8

As explained in Ref 25, the flap inputs create “anti-noise”, in order to cancel out the baseline pulse, by altering the in-plane forces on the rotor blade. The in-plane torque force (c_x) for the baseline case and the force increment from the baseline for the minimum noise flap phasing for 2, 3, 4, and 5P are plotted in Figure 27. An anti-drag pulse (+ c_x , +leading edge) is seen on the advancing blade in all four “best” noise cases. There are clear resemblances and trends between the different flap inputs. These plots can be correlated to the dB reductions

(Figure 25), and noted that the 5P input is more effective than 2P. In fact, for acoustics it is the derivative of the loading that contributes to noise. For the 2, 3, 4, and 5P minimum noise cases, the optimal flap phasings are 330, 240, 150, and 60 deg, respectively. It is interesting to note that in all four “optimum” cases in CFD, the flap is halfway deflected ($1/2 \delta_f$) at 90 deg azimuth and is returning to zero deflection. This does not hold for the test data since the best experimental points are somewhat shifted relative to CFD. However, the decreasing flap deflection at 90 deg azimuth is consistent with increasing section loading, due to the opposite effects of the moment flap. The figure shows that after 90 deg azimuth there is a strong gradient in the in-plane force. Computations by Boyd (Ref. 28) on the HART II rotor have shown similarly good agreement in predicting flap phasing effects on BVI noise.

CONCLUSIONS

Multidisciplinary analyses of an active flap rotor have been performed using CFD/CSD coupling to account for aeroelastics and rotor trim. High performance computing has been used to simulate 0, 2, 3, 4, and 5/rev flap inputs, with 1.5 deg nominal flap deflection and varying flap phase and amplitude. Comparisons have been made with experimental Boeing SMART data and rotocraft comprehensive code lifting-line analysis for airloads, structural loads, control power, performance, and noise. Flow physics and flap gap effects have been investigated. The following conclusion are drawn:

1) The bearingless, flapped SMART rotor with high-fidelity flap gap representations has proven to be a challenge for both CSD modeling and the overset CFD methodology. Numerical convergence, computational efficiency, and solution smoothness and accuracy have been adversely impacted by model complexity. Considerable effort was required in order to faithfully account for flap gaps.

2) Fine grids are required to accurately predict absolute performance for the baseline SMART rotor cruise case. However, coarse grids are shown to be more efficient and as accurate for incremental predictions compared with test data.

3) CFD/CSD analyses indicate that the trimmed SMART rotor shows negligible performance (power/thrust) improvement (or degradation) for various flap schedules, thrust coefficients, and advance ratios. This conclusion is in general agreement with experimental data.

4) CFD/CSD in-plane LFSPL noise increments (dB) due to flap deflection are in excellent agreement with experimental microphone data. CFD aerodynamic results clearly show the in-plane force noise-canceling mechanism. However, absolute acoustic pressure signatures and sound pressure levels are poorly predicted using non-compact on-surface acoustic FW-H analyses.

5) Structural load predictions are generally fair for absolute prediction magnitude and waveform compared with experimental data, while increments from the

baseline show some agreement. CFD/CSD coupling offers little improvement over comprehensive analysis.

6) CFD-computed blade aerodynamics provides more accurate three-dimensional, unsteady, compressible effects compared with the lifting-line aerodynamics. Compared with an unflapped MDART rotor, the flap and flap gaps are seen to reduce outboard loading and increase sectional chord force. Flap tip vortices are accurately depicted. Noticeable differences with comprehensive analysis are seen.

7) Overall, aerodynamic quantities (performance, control power, noise) appear reasonably well predicted, whereas structural loads and vibration require continued research and more thorough investigation into the rotor properties and test data.

This work offers an important advancement in rotorcraft analysis capability for advanced technology, complex geometry rotor configurations under study for future Army rotorcraft.

ACKNOWLEDGEMENTS

Computing resources under a DoD HPCMP Challenge Project at the Navy DSRC are gratefully acknowledged. Dr. Gene Ruzicka contributed to initial setup and debugging of the CFD computations. We thank the NASA Subsonic Rotary Wing Program and the entire SMART Test Team for the data. Assistance from colleagues from NASA (Drs. William Warmbrodt, Wayne Johnson, Sesi Kottapalli, and Mr. Benton Lau), Georgia Tech (Jeremy Bain), University of Maryland (Dr. Shreyas Ananthan), Boeing (Dr. Friedrich Straub), and UARC/AFDD (Dr. Ben Sim) is very much appreciated. Dr. Doug Boyd provided invaluable assistance and insight with WOPWOP, as well as the OVERFLOW to WOPWOP non-compact loading converter.

REFERENCES

1. Yeo, H., "Assessment of Active Controls for Performance Enhancement," *Journal of the American Helicopter Society*, Vol. 53, No. 2, April 2008, pp. 152-163.
2. Kottapalli, S., "Low-Speed and High-Speed Correlation of SMART Active Flap Rotor Loads," AHS Aeromechanics Specialists' Conference, San Francisco, CA January 2010.
3. Liu, L., Friedmann, P. P., Kim, I., and Bernstein, D. S., "Simultaneous Vibration Reduction and Performance Enhancement in Rotorcraft Using Actively Controlled Flaps", AHS 62nd Annual Forum, Phoenix, AZ, May 2006.
4. Fulton, M. V., "Aeromechanics of the Active Elevon Rotor," AHS 61st Annual Forum, Grapevine, TX, June 2005.
5. Gagliardi, A., Beedy, J., Steijl, R., Barakos, G., and Badcock, K., "Analysis of Flapped Rotors Using CFD and Indicial Methods," AHS 61st Forum, Grapevine, TX, June 2005.
6. Aoyama, T., Yang, C., and Saito, S., "Numerical Analysis of Active Flap for Noise Reduction Using Moving Overlapped Grid Method," AHS 61st Forum, Grapevine, TX, June 2005.
7. Jain, R., Szema, K-Y., Munipalli, R., Yeo, H., and Chopra, I., "CFD-CSD Analysis of Active Control of Helicopter Rotor for Performance Improvement," AHS 65th Annual Forum, Grapevine, TX, May 2009.
8. Ananthan, S., and Baeder, J., "Prediction and Validation of Loads on Bearingless Rotors Using a Coupled CFD-CSD Methodology," AHS 64th Forum, Montreal, Canada, April 2008.
9. Bain, J., Potsdam, M., Sankar, L., and Brentner, K. S., "Aeromechanic and Aeroacoustic Predictions of the Boeing SMART Rotor Using Coupled CFD/CSD Analysis," AHS 66th Forum, Phoenix, AZ, May 2010.
10. Potsdam, M., Fulton, M., Dimanlig, A., and Sim, B., "Multidisciplinary Coupling for Active Flapped Rotors," High Performance Computing Modernization Program User's Group Conference, San Diego, CA, June 2009.
11. Mishra, A., Sitaraman, J., Baeder, J., and Opoku, D., "Computational Investigation of Trailing Edge Flap for Control of Vibration," AIAA Paper 2207-4290, 25th AIAA Applied Aerodynamics Conference, Miami, FL, June 2007.
12. Straub, F., Anand, V., Birchette, T., and Lau, B., "Wind Tunnel Test of the SMART Active Flap Rotor," AHS 65th Forum, Grapevine, TX, May 2009.
13. Delrieux, Y., Le Pape, A., Leconte, P., Crozier, P., Gimonet, B., and Mercier des Rochettes, H., "Wind-Tunnel Assessment of the Concept of Active Flaps on a Helicopter Rotor Model," AHS 63rd Annual Forum, Virginia Beach, VA, May 2007.
14. Koratkar, N., and Chopra, I., "Wind Tunnel Testing of a Mach-Scaled Rotor Model with Trailing-Edge Flaps," Smart Materials and Structures, Vol. 10. pp. 1-14, 2001.
15. Fulton, M. V., and Ormiston, R. A., "Small-Scale Rotor Experiments with On-Blade Elevons to Reduce Blade Vibratory Loads in Forward Flight," AHS 54th Annual Forum, Washington, DC, May 1998.
16. Potsdam, M., Yeo, H., and Johnson, W., "Rotor Airloads Prediction Using Loose Aerodynamic/Structural Coupling," *Journal of Aircraft*, Vol. 43, No. 3, May-June 2006, pp. 732-742.
17. Ananthan, S., Baeder, J., Sitaraman, J., Hahn, S., and Iaccarino, G., "Hybrid Unsteady Simulation of Helicopters: HUSH," AIAA Paper 2008-7339, 26th AIAA Applied Aerodynamics Conference, Honolulu, HI, August 2008.
18. Duque, E. P., N., Sankar, L., Menon, S., Bauchau, O., Ruffin, S., Smith, M., Ahuja, A., Brentner, K., Long, L., Morris, P., and Gandhi, F., "Revolutionary Physics-Based Design Tools for Quiet Helicopters," AIAA Paper 2006-1068, 44th AIAA Aerospace Sciences Meeting and Exhibit, Reno, NV, January 2006.
19. Hall, S., Anand, V., Straub, F., and Lau, B., "Active Flap Control of the SMART Rotor for

- Vibration Reduction," AHS 65th Forum, Grapevine, TX, May 2009.
20. Jacklin, S., Lau, B., Nguyen, K., Smith, R., and McNulty, M., "1994 Full-scale Wind Tunnel of the McDonnell-Douglas five-bladed Advanced Bearingless Rotor: Performance, Stability, Loads, Control Power, Vibration, and HHC Data," American Helicopter Society Aero-mechanics Specialists' Conference, San Francisco, CA, January 1994.
21. Johnson, W., "Technology Drivers in the Development of CAMRAD II," American Helicopter Society Aero-mechanics Specialists' Conference, San Francisco, CA, January 1994.
22. Strawn, R., Nygaard, T., Bhagwat, M., Dimanlig, A., Saberi, H., Ormiston, R., and Potsdam, M., "Integrated Computational Fluid and Structural Dynamics Analyses for Comprehensive Rotorcraft Analysis," AIAA Paper 2007-6575, AIAA Atmospheric Flight Mechanics Conf., Hilton Head, SC, August 2007.
23. Bain, J., Sankar, L., Erwin, J., and Brentner, K., "Application of Overset Grids to the Boeing SMART Rotor Using Chimera Grid Tools," 9th Symposium on Overset Composite Grid and Solution Technology, State College, PA, October 2008.
24. Cheng, R., Theodore, C., and Celi, R., "Effects of Two/rev Higher Harmonic Control on Rotor Performance," *Journal of the American Helicopter Society*, Vol. 48, No. 1, pp. 18-27, January 2003.
25. Sim, B., JanakiRam, R., Barbely, N., and Solis, E., "Reduced In-Plane, Low Frequency Noise of an Active Flap," AHS 65th Forum, Grapevine, TX, May 2009.
26. Yu, Y., Tung, C., van der Wall, B., Pausder, H., Burley, C., Brooks, T., Beaumier, P., Delrieux, Y., Mercker, E., and Pengel, K., "The HART-II Test: Rotor Wakes and Aeroacoustics with Higher-Harmonic Pitch Control (HHC) Inputs – The Joint German/French/Dutch/US Project," AHS 58th Annual Forum, Montreal, Canada, June 2002.
27. Shirey, J. S., Brentner, K. S., Chen, H.-N., "A Validation Study of the PSU-WOPWOP Rotor Noise Prediction System," AIAA Paper 2007-1240, 45th AIAA Aerospace Sciences Meeting and Exhibit, Reno, NV, January 2007.
28. Boyd, D. D., "HART II Acoustic Predictions Using a Coupled CFD/CSD Analysis," American Helicopter Society 65th Annual Forum, Grapevine, TX, May 2009.
29. Sim, B., Potsdam, M., Connor, D., and Watts, M., "Direct CFD Predictions of Low Frequency Sounds Generated by Helicopter Main Rotors," AHS 66th Annual Forum, Phoenix, AZ, May 2010.
30. Rajmohan, N., Sankar, L., N., Makinen, S., Egolf, T. A., and Charles, B., D., "Application of Hybrid Methodology to Rotors in Steady and Maneuvering Flight," AMS 65th Annual Forum, Grapevine, TX, May 2009.



Figure 1. SMART rotor including flap

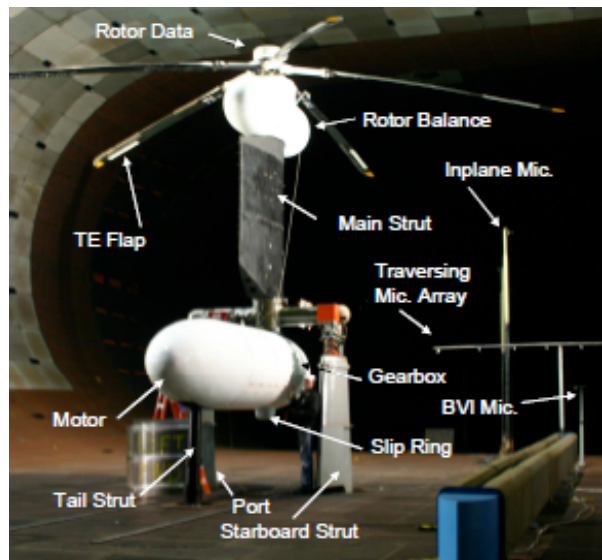


Figure 2. SMART rotor in NFAC 40x80-Ft. Wind Tunnel

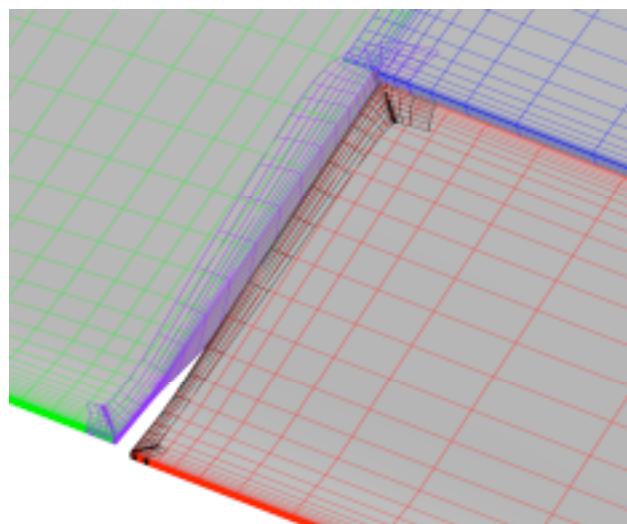
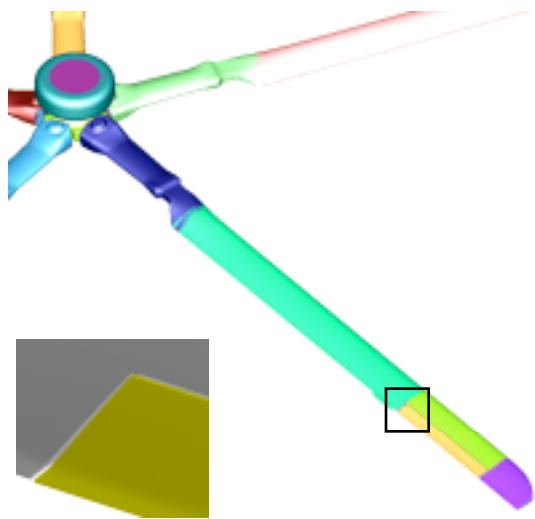


Figure 3. SMART overset surface CFD grid system (flap edge inset)

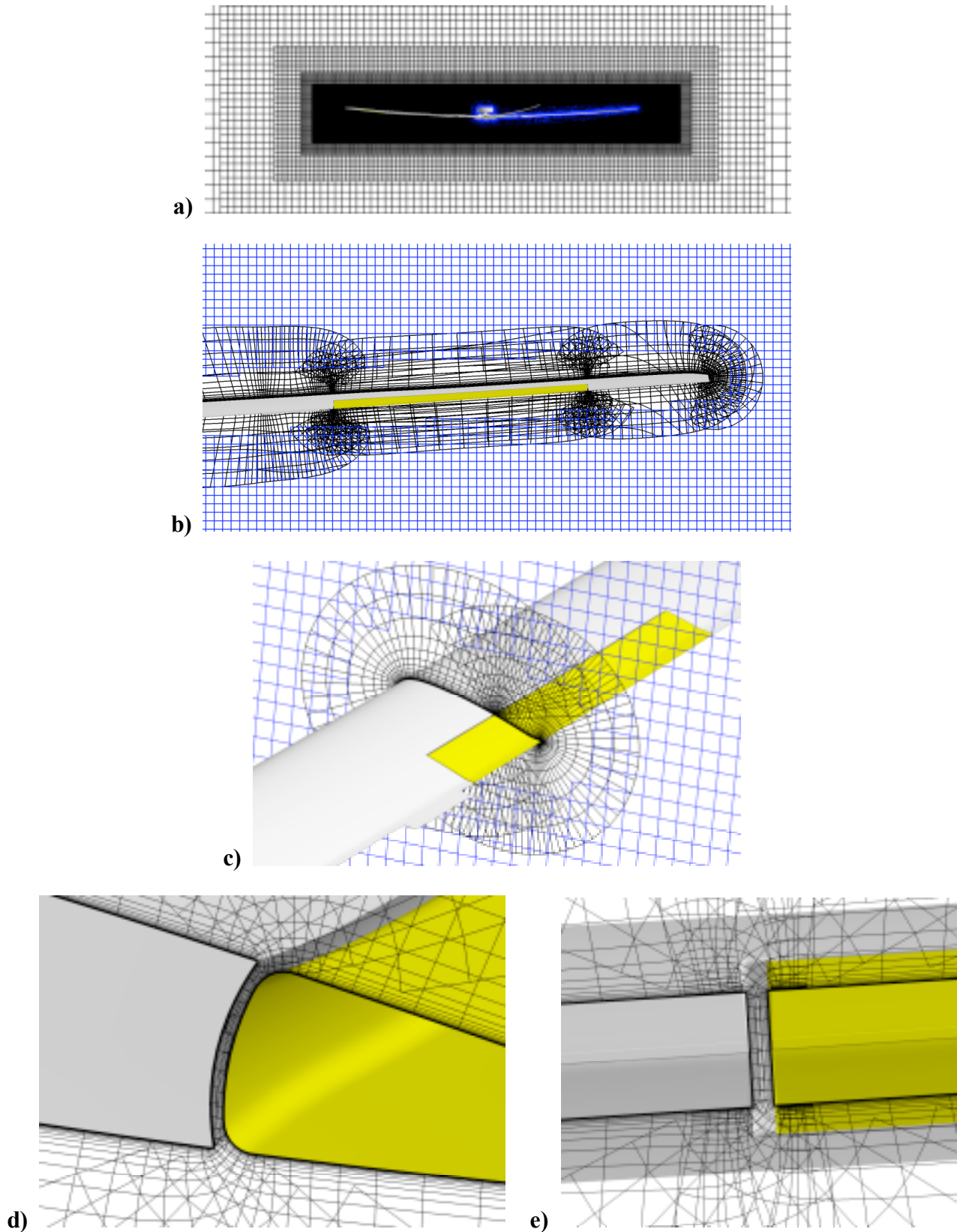


Figure 4. SMART overset volume CFD grid system: a) overall, b) outboard, c) flapped section, d) chordwise flap gap, e) spanwise flap gap (rear view)

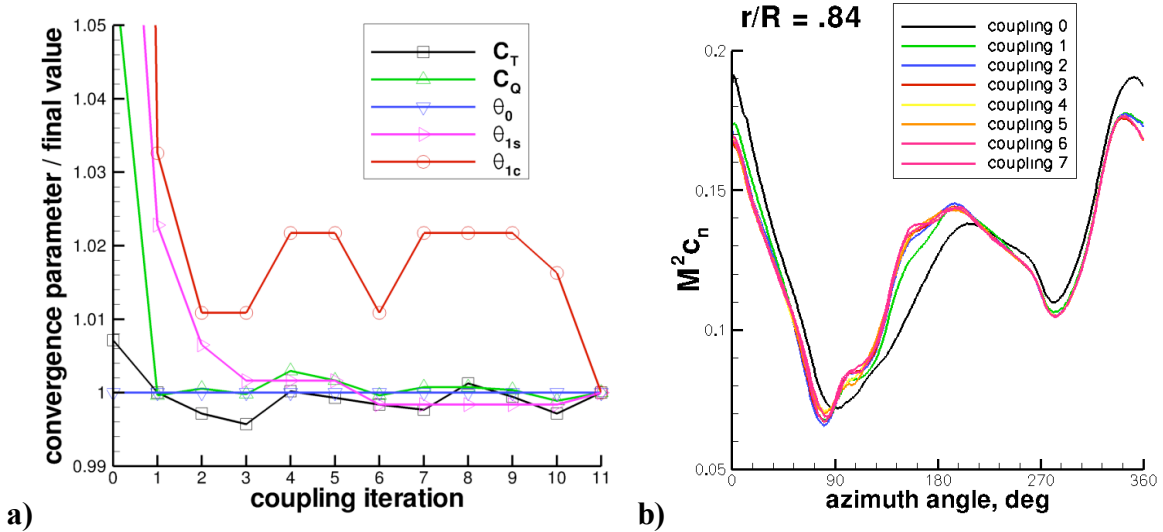


Figure 5. SMART baseline CFD/CSD coupling convergence: a) pitch controls and rotor performance, b) section normal force at 84% R

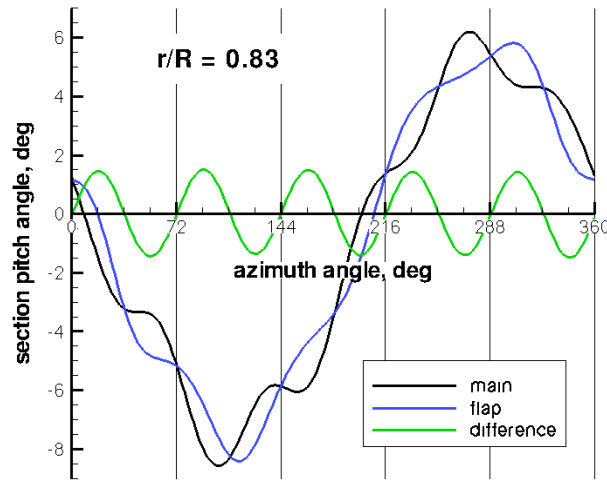


Figure 6. SMART main and flap motion specification, 5P/1.5°/0°, section pitch at 83% R

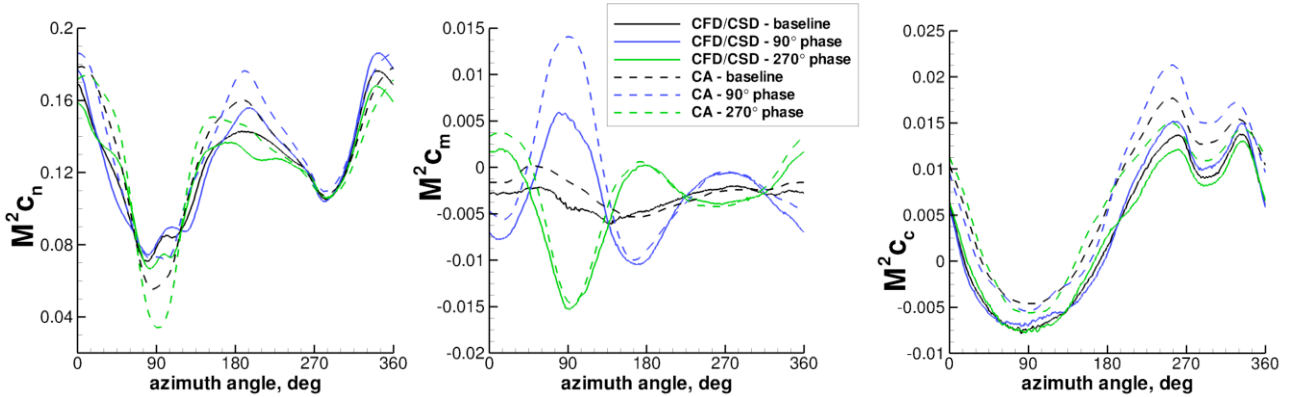


Figure 7. Airloads (normal force, pitching moment, and chord force) at 84% R, CFD/CSD and CA; baseline, 2P/1.5°/90°, 2P/1.5°/270°

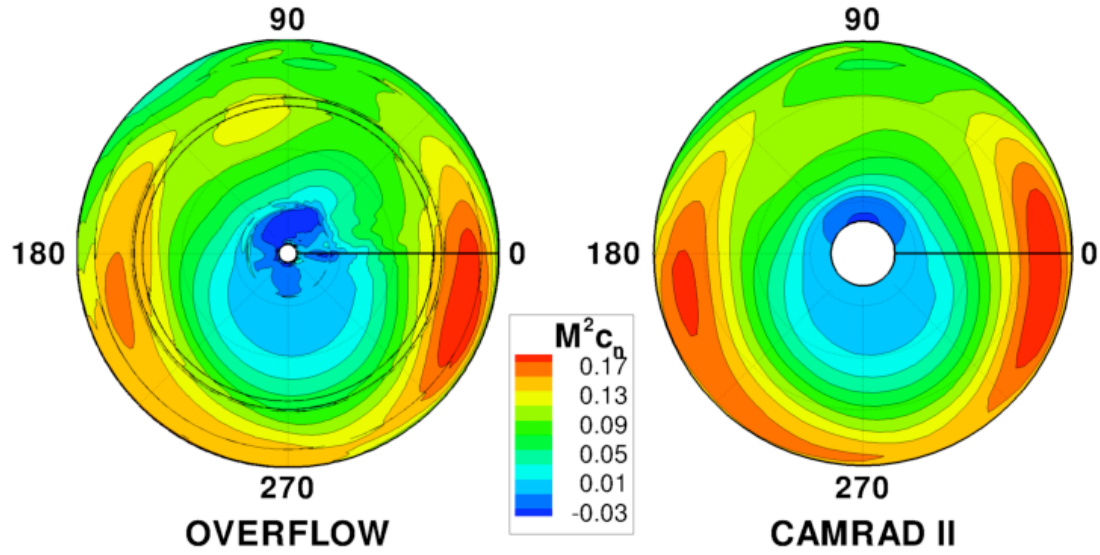


Figure 8. Normal force disk loading, baseline, CFD/CSD and CA

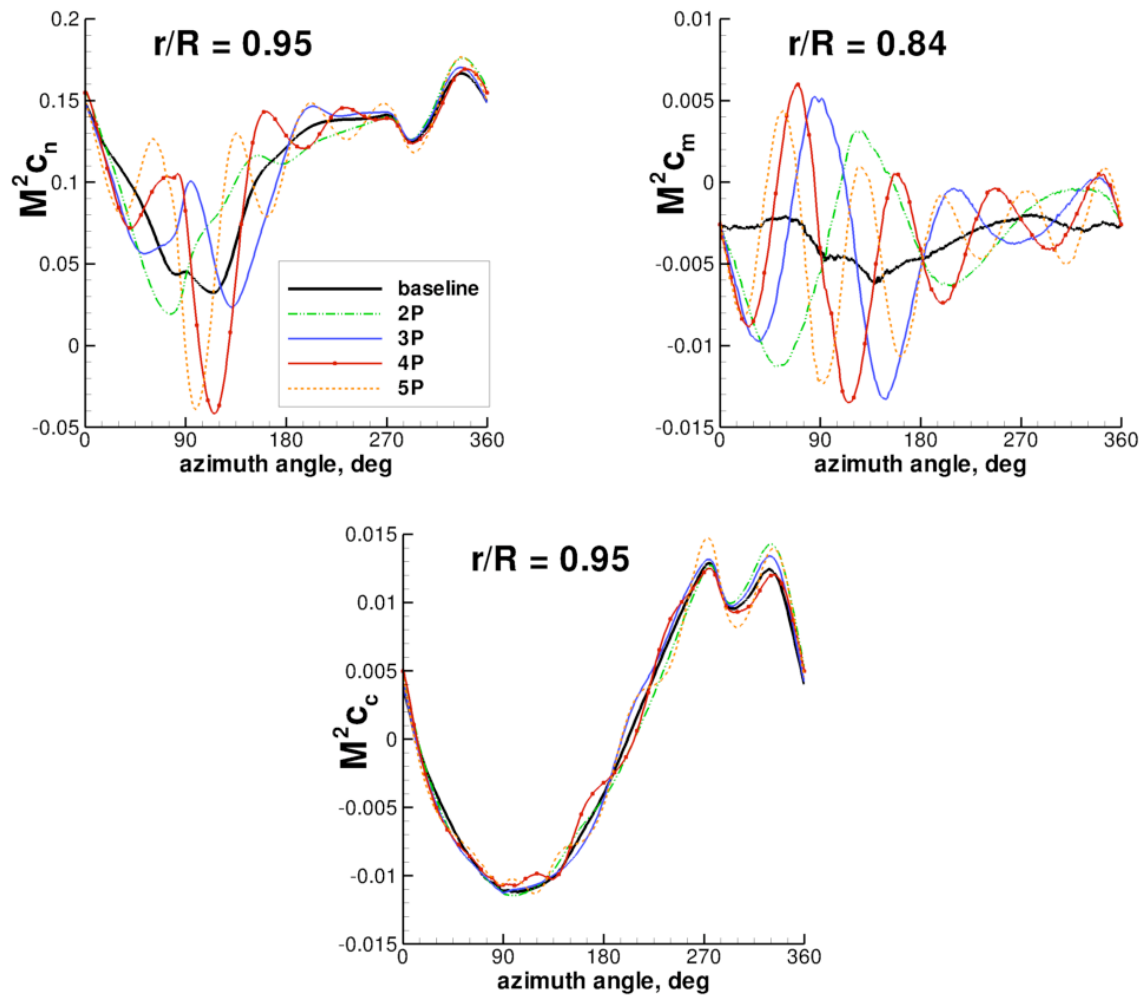


Figure 9. Airloads (normal force, pitching moment, chord force), 2 – 5P/1.5°/0°, CFD/CSD

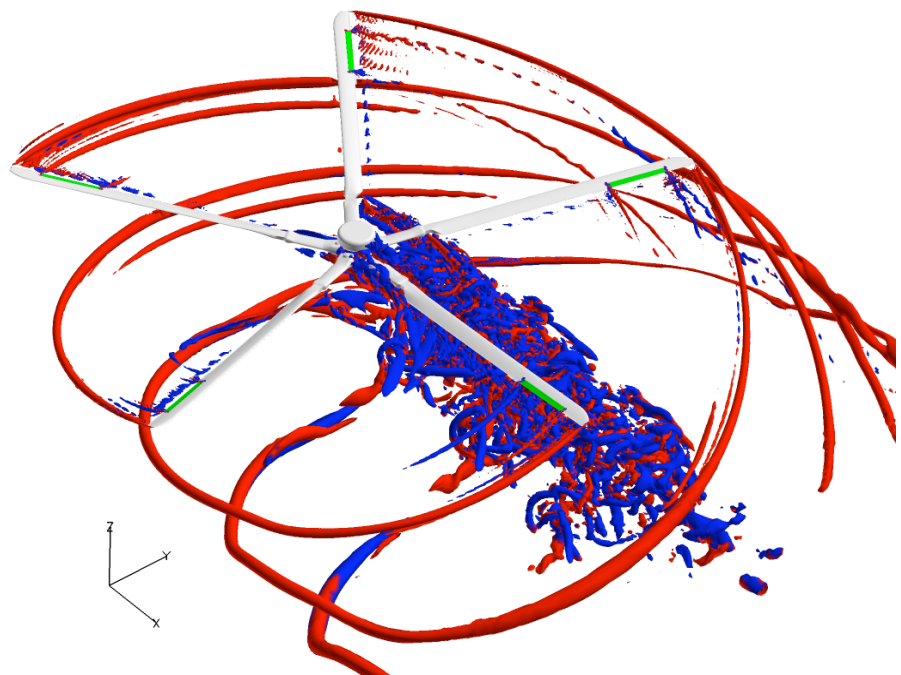


Figure 10. CFD wake visualization: Q criteria iso-surface colored by vortex rotation sense, 2P/1.5°/90°, fine grid

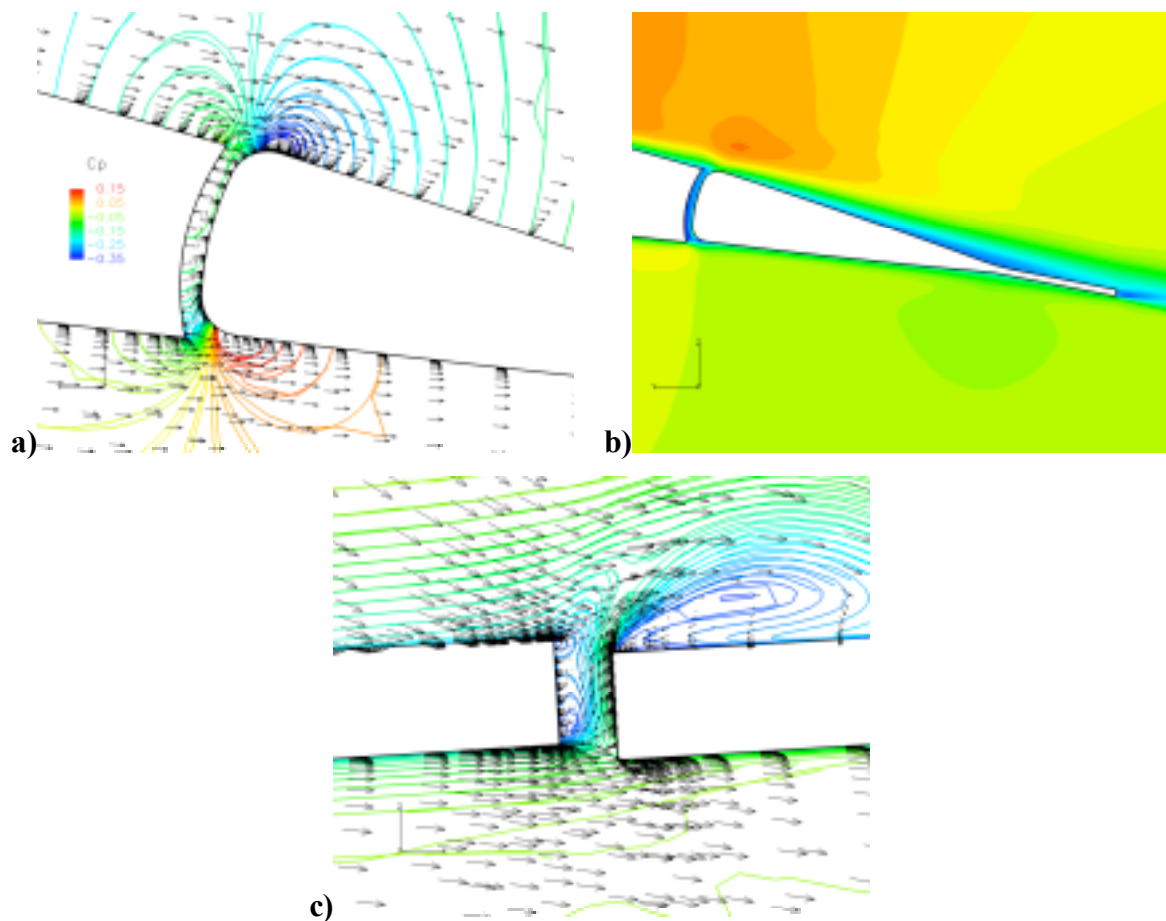


Figure 11. Flap gap flow: a) chordwise gap c_p contours and velocity vectors, b) chordwise gap velocity contours, c) spanwise gap c_p contours and velocity vectors

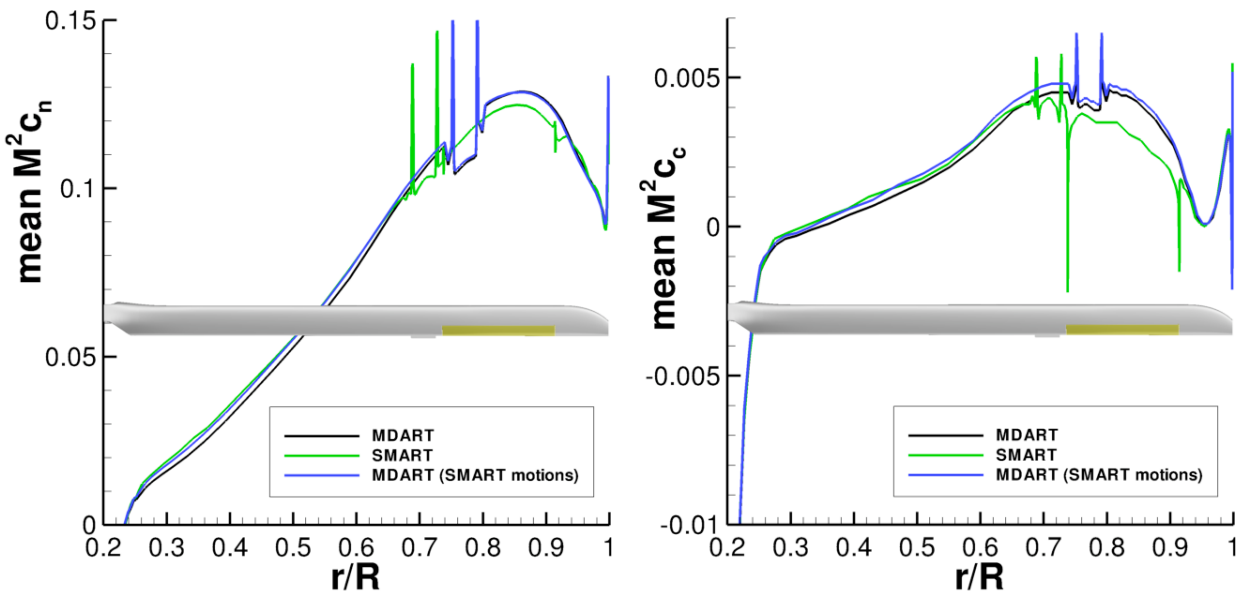


Figure 12. Mean airloads (normal force, chord force) for MDART, SMART, and MDART with SMART motions (c_c +leading edge)

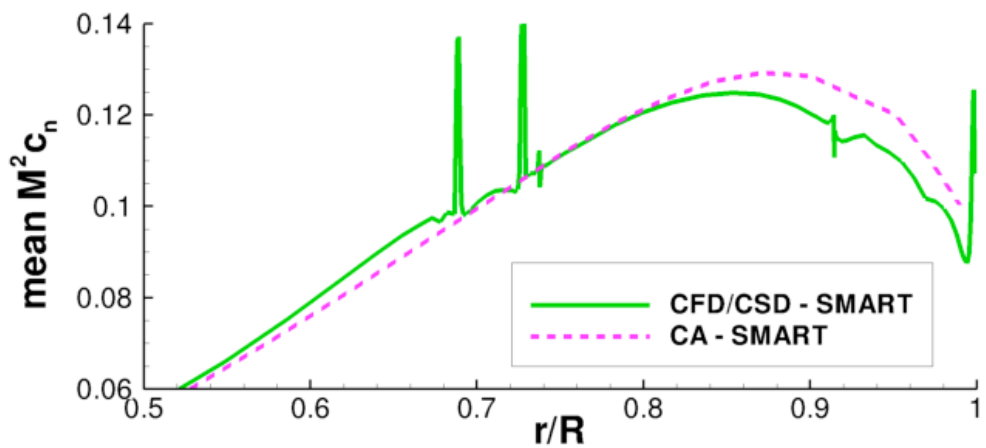


Figure 13. Mean outboard normal force for SMART, CFD/CSD and CA, baseline

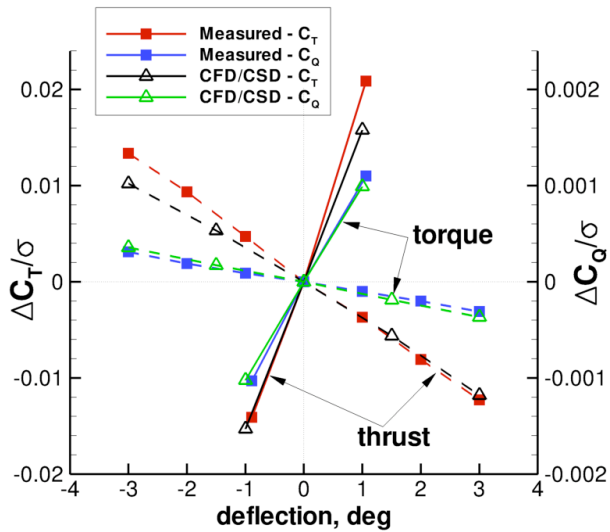


Figure 14. Control power: change in thrust and torque with collective pitch (solid lines) and flap deflection (dashed lines)

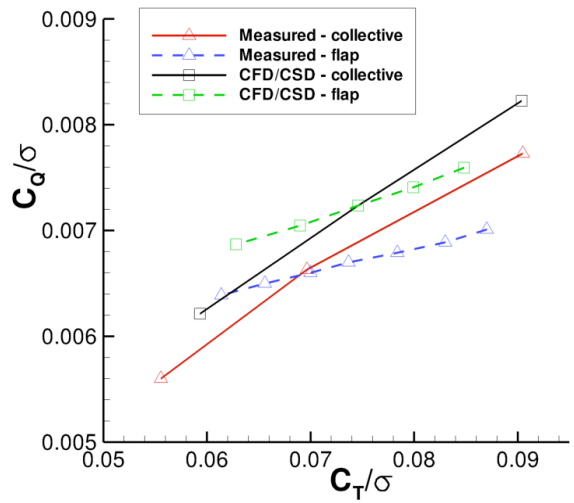


Figure 15. Control power: thrust vs. torque for collective pitch (solid lines) and flap deflection (dashed lines)

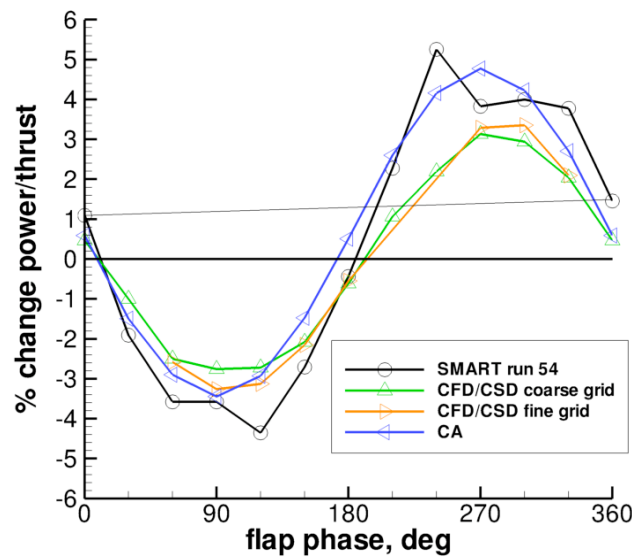


Figure 16. Power/thrust performance increment vs. flap phasing, 2P/1.5°, fixed controls

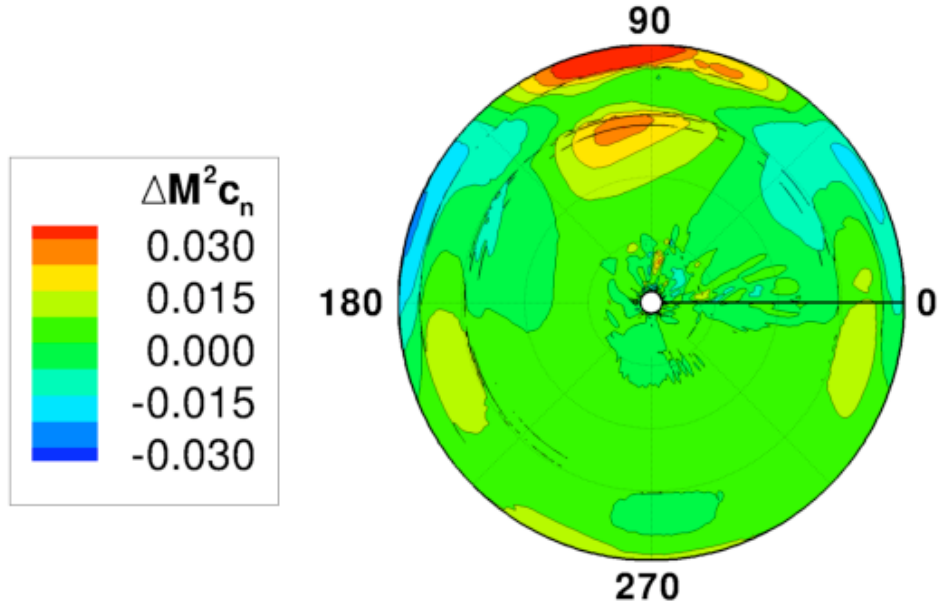


Figure 17. CFD/CSD normal force increment from baseline, 2P/1.5°/90°, fixed controls

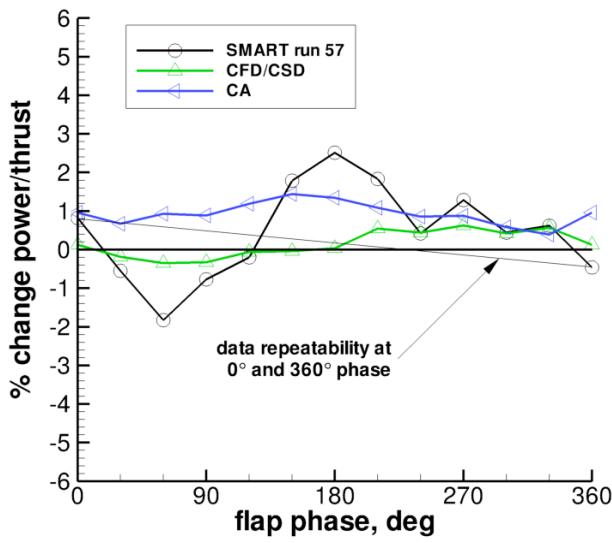


Figure 18. Power/thrust performance increment vs. flap phasing, 2P/1.5°, trimmed, baseline flight conditions

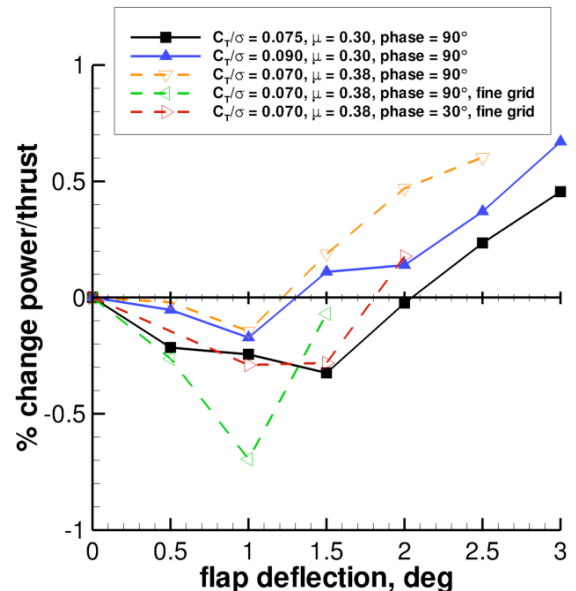


Figure 19. Power/thrust performance increment vs. flap deflection, 2P, trimmed, various flight conditions, CFD/CSD only

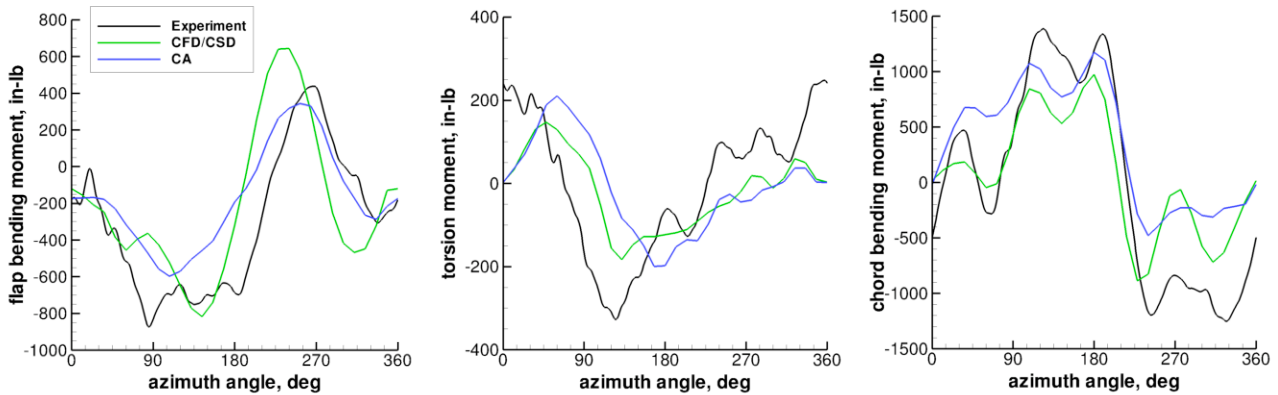


Figure 20. Flap-wise bending (59% R), torsion moment (64% R, mean removed), and chord-wise bending moment (59% R, mean removed), baseline

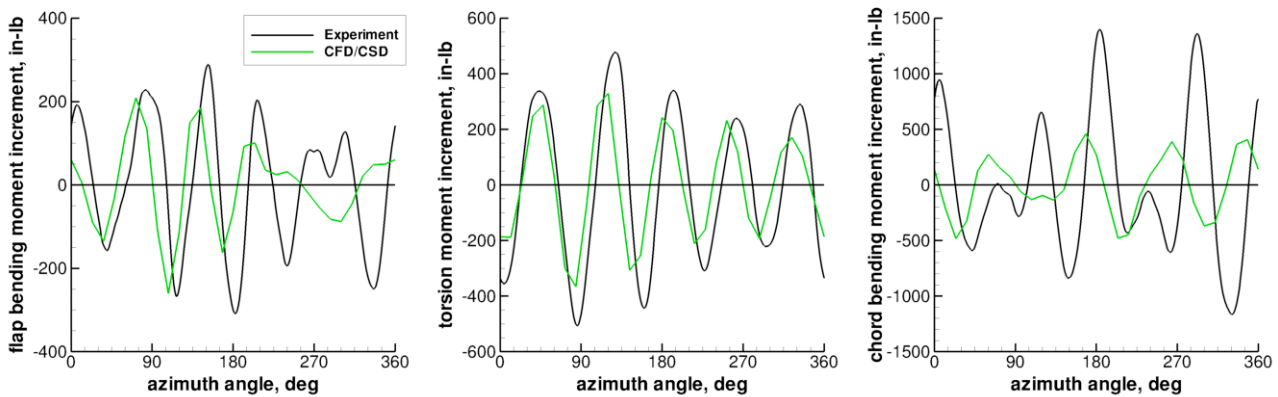


Figure 21. Flap-wise bending (59% R), torsion moment (64% R), and chord-wise bending moment (59% R), 5P/1.5°/90° minus baseline, mean removed

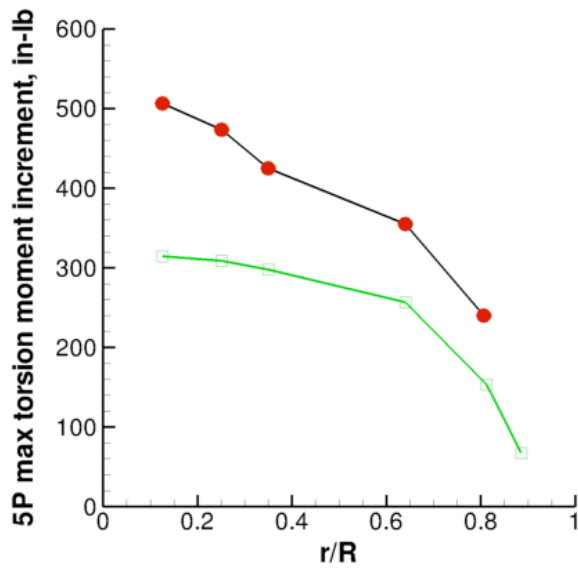
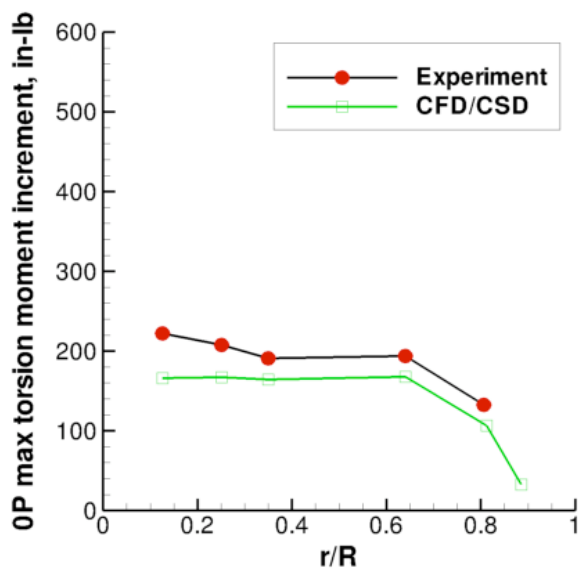


Figure 22. Maximum torsion moment increment, 0P and 5P, 1.5° deflection, various phase

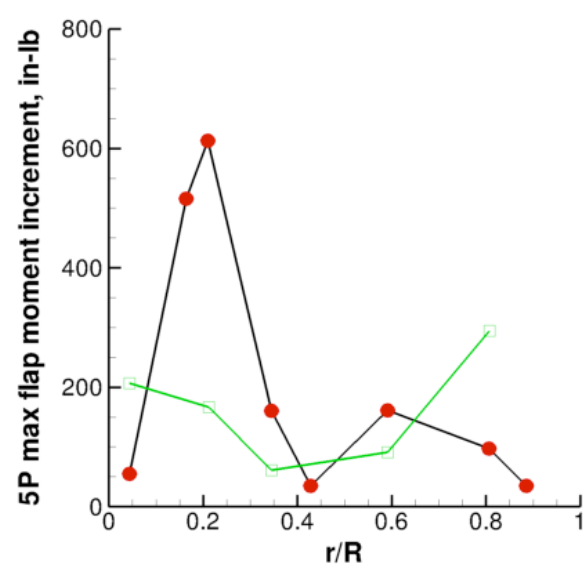
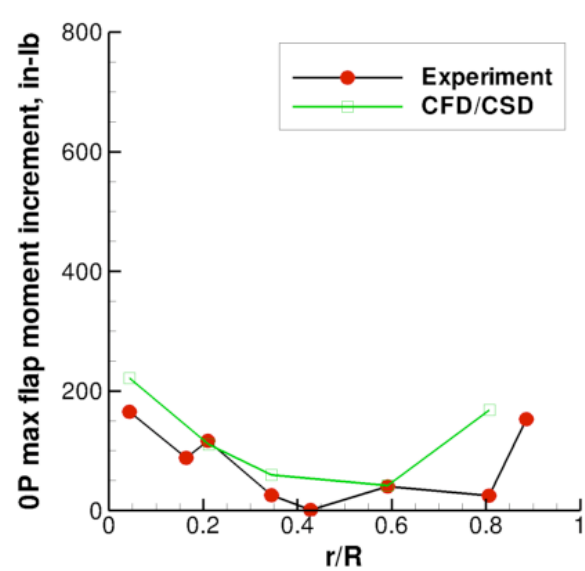


Figure 23. Maximum flap bending moment increment, 0P and 5P, 1.5° deflection, various phase

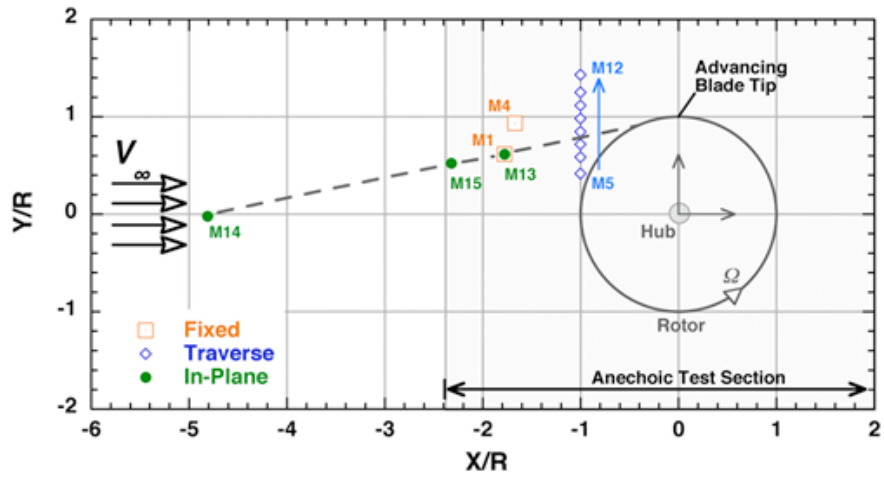


Figure 24. SMART in-plane microphone location 13 (M13) in the NFAC (Ref. 25)

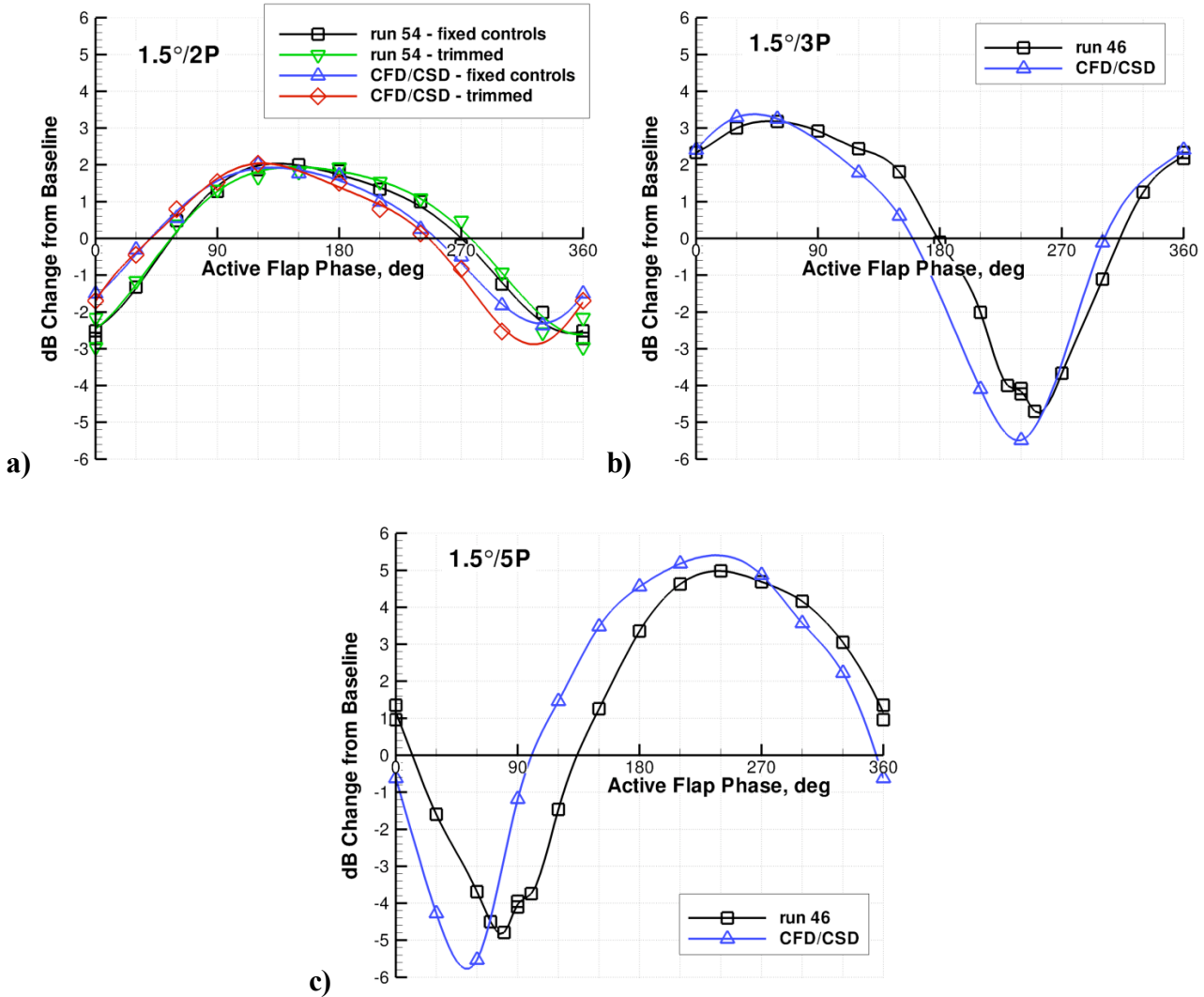


Figure 25. In-plane LFSPL noise increment (dB) vs. flap phase for a) 2P, b) 3P, and c) 5P inputs

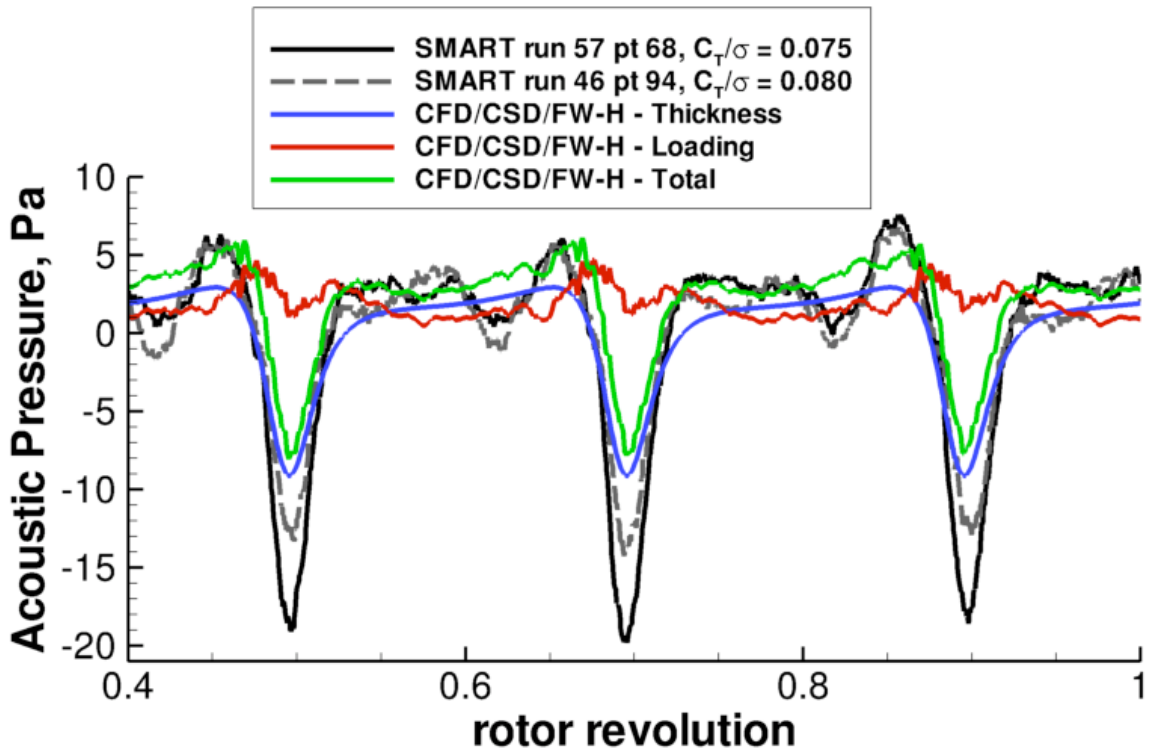


Figure 26. Acoustic pressure signal from experiment and Ffowcs-Williams Hawking analysis, baseline

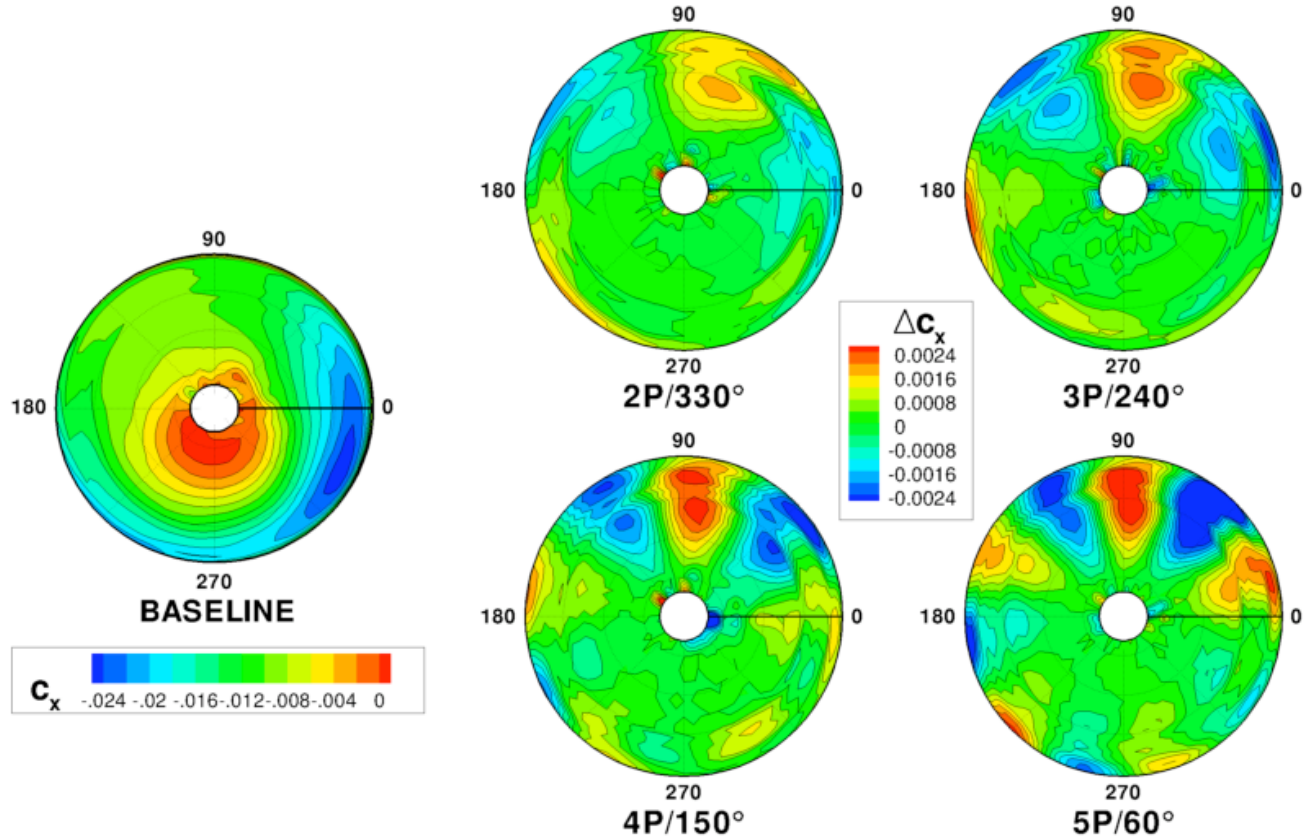


Figure 27. In-plane section airloads (c_x): a) baseline, b) differential from baseline for “best” noise – 2P/1.5°/330°, 3P/1.5°/240°, 4P/1.5°/150°, and 5P/1.5°/60°, (c_x + leading edge)